Observation of surface magnons and crystalline electric field shifts in superantiferromagnetic NdCu 2 nanoparticles

Article · October 2021

DOI: 10.1103/PhysRevB.104.134404

CITATIONS
0

READS
125

7 authors, including:

Elizabeth Martín Jefremovas
Universidad de Cantabria
7 PUBLICATIONS **12** CITATIONS
SEE PROFILE

Andreas Michels
University of Luxembourg
139 PUBLICATIONS **2,187** CITATIONS
SEE PROFILE

Jesus A. Blanco
University of Oviedo
338 PUBLICATIONS **3,591** CITATIONS
SEE PROFILE

Luis Fernández Barquín
Universidad de Cantabria
191 PUBLICATIONS **2,363** CITATIONS
SEE PROFILE

Observation of surface magnons and crystalline electric field shifts in superantiferromagnetic $NdCu_2$ nanoparticles

E. M. Jefremovas,[1,*] M. de la Fuente Rodríguez,[1] F. Damay,[2] B. Fåk,[3] A. Michels,[4] J. A. Blanco,[5] and L. F. Barquín[1]

[1]*Dpto. CITIMAC, Facultad de Ciencias, Universidad de Cantabria, 39005 Santander, Spain*

[2]*Laboratoire Léon Brillouin, CEA-CNRS, 91191 Gif-sur-Yvette Cedex, France*

[3]*Institut Laue-Langevin, 38042 Grenoble Cedex 9, France*

[4]*Department of Physics and Materials Science, University of Luxembourg, L-1511 Luxembourg, Grand Duchy of Luxembourg*

[5]*Department of Physics, University of Oviedo, 33007 Oviedo, Spain*

(Received 30 March 2021; revised 22 August 2021; accepted 27 September 2021; published 8 October 2021)

An ensemble of superantiferromagnetic $NdCu_2$ nanoparticles has been produced to perform a detailed analysis of magnetic excitations using inelastic neutron scattering. Neutron diffraction measurements indicate a mean nanoparticle size of $\langle D \rangle \approx 13$ nm, where the bulk commensurate antiferromagnetic structure is retained at the nanoparticle core. Magnetic measurements evidence the interaction among the magnetic moments located at the nanoparticle surface to be strong enough to establish a spin glass behavior. Specific heat analyses show a broad Schottky contribution, revealing the existence of a crystalline electric field. Inelastic neutron scattering analyses disclose that the splitting of the crystalline electric field levels associated with the Nd^{3+} ions, as well as the spin-wave excitations that emerged below the Néel transition ($T_N \approx 6$ K) in polycrystalline $NdCu_2$ are maintained in the nanoparticle state. We have been able to isolate the scattering contribution arising from the nanoparticle surface where both crystalline electric field splitting and the collective magnetic excitations are well-defined despite the symmetry breaking. Quantitative analyses of this surface scattering reveal that finite-size effects and microstrain lead to a partial inhibition of the transitions from the ground state to the first excited level, as well as a positive shift (∼15%) of the energy associated to collective magnon excitations.

DOI: 10.1103/PhysRevB.104.134404

I. INTRODUCTION

Research on magnetic nanoparticles (MNPs) has already become mature [1,2] and the ensuing technology transfer, especially in data storage, sensing, and biomedicine, has boosted broad interest in the last two decades [3–6]. Although the influence of the MNP size and/or shape [7] in the magnetic properties has been thoroughly studied in 3*d* core/shell MNPs [8], some subtleties have remained hidden until recently. These are the effects of the magnetic anisotropy [9] or the magnetic disorder and interparticle coupling in superspin glass and superferromagnetic systems [10,11]. Even more, ferromagnetically coupled entities, rather than magnetic moments within NPs (the so-called *supraferromagnetic correlations* [11]) have been revealed in clusters of MNPs [12]. All these manifestations of magnetism are intricately connected to the presence of defects, which are intrinsic to nanocrystalline materials, already considered a new class of disordered solids [13]. The existence of defects, strained lattices, and surfaces in MNPs has crucial consequences on the magnetic static arrangements and moment dynamics. This is not surprising, considering that very recent studies underline the role of interfacial zones (boundaries) in which a change of atomic periodicity gives rise to unexpected electric and/or magnetic behaviors [14–16].

In the last decades, RX_2 MNPs (where R stands for rare earth) have revealed advantages to easily tuning the magnetic coupling (ferro- or antiferromagnetic) by simply changing R or the nonmagnetic metal (X) [17,18]. When it comes to collective excitations, only a few studies have shown direct evidence of the presence of spin waves in ensembles of MNPs of hematite and maghemite [19–21] by inelastic neutron scattering (INS), even if the propagation of spin waves is attracting a lot of attention nowadays [22,23]. However, little is known about the crystalline electric field (CEF) effects in $4f$-MNPs, apart from nanocrystalline pure Tb [24], nonperiodic $TbCd_6$ quasicrystals [25], and multilayers [26]. The influence of particle size, microstrain, and surface effects on the CEF and the magnetic excitations in general remains essentially unexplored.

To fill in this gap, in this paper, we have studied the CEF excitations in the paramagnetic (PM) state and the magnetic excitations in the magnetically ordered phase of an ensemble of superantiferromagnetic (SAFM) MNPs of $NdCu_2$ by using INS. These ensembles of MNPs consist of small antiferromagnetically ordered entities (cores) that get connected to each other via the spin glass (SG) disordered surface, which is a result of the uncompensated AFM moments in the vicinity of the surface and taking into account the random anisotropy model [27,28]. It is worth mentioning that the determination and understanding on how the bulk collective excitations develop at the nanoscale is of basic interest in condensed matter physics. Moreover, it is a must to define the role that the core

*Corresponding author: martinjel@unican.es

and the surface/interface part of the MNPs are playing in the moment dynamics. This is at the basis of several problems concerning quantum magnetism (e.g., Refs. [29–31]). In addition, the findings for these $4f$ MNPs will complete those previously studied in ensembles of Fe-oxide MNPs [19,32,33].

II. EXPERIMENTAL DETAILS

Polycrystalline pellets of $NdCu_2$ have been produced using an arc furnace (MAM-1, Johanna Otto Gmbh) under an Ar atmosphere (99.99%). The alloys were sealed off under Ar pressure (99.99%) and nanoscaled via ball milling (high-energy planetary Retsch PM 400/2). We have selected milling times $t = 2$ and 5 h, as our previous experience indicates these t to be enough to achieve NP sizes $\langle D\rangle$ around 10 nm [17,34,35]. Although size dispersion is inherent to the milling route, the aforementioned works have reported size dispersion values that are always less than 15% [36], which is, for the aim of this paper, more than enough. In this way, this paper aims to track the changes that take place in the NP state compared to the bulk situation, i.e., not to focus on a particular MNP size. Therefore, a size dispersion does not hamper the main results provided in this paper. On the contrary, the use of this grinding technique is crucial to the need to access the sufficient amount of MNPs ($\sim$ 12 g MNPs for each milling time) required for measurements.

The structural characterization has been performed by employing x-ray diffraction (XRD) and neutron diffraction (ND). The former were performed at room temperature in a Bruker D8 Advance diffractometer using Cu-Kα ($\lambda = 1.5418$ Å) radiation. The ND patterns were collected at G4.1 instrument (LLB, France) using a wavelength $\lambda = 2.426$ Å at several temperatures between $T = 1.5$ K and 15 K. A measuring time of 8 h for each pattern has been used to assure a high signal-to-noise ratio.

The magnetic characterization (static $M_{\rm DC}(T, \mu_0 H)$ and dynamic $\chi_{\rm AC}(T, f)$) was performed in both Quantum Design QD–PPMS and QD–MPMS (SQUID) magnetometers within the temperature range of $T = 2$–300 K and magnetic fields $\mu_0 H \leqslant 5$ T. The dynamic $\chi_{\rm AC}(T, f)$ behavior was analyzed using an oscillating field $\mu_0 H = 0.313$ mT and frequencies (f) ranging from 0.1 kHz to 10 kHz in the 2–10 K range. No DC-bias field was applied during the measurements.

Heat-capacity measurements were performed on compacted disks ($\sim$ 5 mg) following the relaxation method [37] under no external applied field within the temperature range of 2–300 K. This technique has allowed us to achieve more information on how the short-range collective excitations that were already present in the bulk alloy survive in the NP state.

INS measurements were made on 5-h milled $NdCu_2$ MNPs, using the neutron time-of-flight spectrometer (IN4, ILL, France) with incident energies of $E_0 = 8.8$, 16.7, and 66.7 meV. We have focused on two temperature values, $T =$ 10 and 1.5 K, which, according to the magnetic characterization, correspond to the PM and magnetic state, respectively. All spectra were corrected for background, absorption, and self-shielding, and normalized to vanadium.

III. RESULTS AND DISCUSSION

Bulk $NdCu_2$ crystallizes in the orthorhombic $CeCu_2$-type structure with space group *Imma* (No. 74). The magnetic ion presents a $4f$ pancakelike electron cloud and below $T_N =$ 6.5 K, antiferromagnetic order, with complex metamagnetic transitions [38]. The CEF description of polycrystalline bulk $NdCu_2$ was originally evaluated by Gratz *et al.* [39], providing values for the nine crystalline field parameters B_l^m (l =2, 4, 6 and m =0, 2, 4, 6 with $m \leqslant l$), with numerical values in the range between 1.2×10^{-5} and 0.134 meV [39]. These are going to be taken as the reference values to check whether they become altered or not in the NP state. To accomplish this, we will first provide the structural and magnetic characterization, as well as the specific heat c_P analyses used to access more information regarding short-range correlations. These results are grouped in a section labeled Preliminary Characterization. Then, the INS data and analyses are provided to unveil the propagation of collective excitations in the nanoscale.

A. Preliminary characterization

1. Structural characterization

According to the crystallographic characterization (XRD included in Ref. [40]), values of mean MNP size and microstrain are obtained as $\langle D\rangle = 18.3(1.0)$ nm and $\eta = 0.62(7)\%$ for $t = 2$ h and $\langle D\rangle = 13.0(5)$ nm and $\eta = 0.59(1)\%$ for $t =$ 5 h-milled $NdCu_2$ MNPs, respectively. As can be seen, the η values lie below 1% in all cases, which ensures the good degree of crystallinity of the MNPs, in spite of the existence of a certain degree of microstrain. This distortion affects the whole MNP, although it gets, of course, stronger at the MNP surface, where interfaces are formed.

Figure 1 includes the measured ND patterns together with the Rietveld refinements (Thompson-Cox-Hastings equations [41]). There, for the PM region [see Figs. 1(a) and 1(c)], the Rietveld refinements give a mean MNP size of $\langle D\rangle = 16.5(4)$ nm (Bragg factor $R_B = \sum_i |I_i - I_i^{\rm calc}| / \sum_i |I_i| = 2.6\%$) for 2 h milled MNPs and $\langle D\rangle = 12.7(1)$ nm ($R_B = 2.4\%$) for 5 h-milled MNPs. These values are in good agreement with the XRD characterization. It is worth noting the occurrence of a magnetoelastic effect, as the unit cell volume V contraction is affected by the magnetic state of the MNPs. In this way, the decrease rate $\frac{\Delta V}{\Delta T}$ is $\approx$ 42 times and 33 times greater for $T < T_N$ than for $T > T_N$ (PM state). This magnetoelasticity that is common in RCu_2 intermetallics [39,42] softens for t =5 h milled MNPs due to the reduction of the number of AFM-coupled magnetic moments, driven by the increase of the lattice mismatch [43,44].

Figures 1(b) and 1(d) concern the magnetic state ($T =$ 1.5 K). For both ensembles of MNPs, the emergence of magnetic Bragg peaks associated with an AFM structure can be observed, especially in the region $18.5^\circ < 2\theta < 24^\circ$ (see the insets). Given that the magnetic unit cell ($\sim$43 Å) is slightly smaller than the MNP core radius ($\sim$45 Å), an AFM arrangement for the magnetic moments within the core is, then, expected [45]. Both the sharpness and the scattering intensities of these magnetic peaks are reduced with respect to the bulk as a result of finite-size effects. Our magnetic Rietveld refinements indicated that the nuclear size,

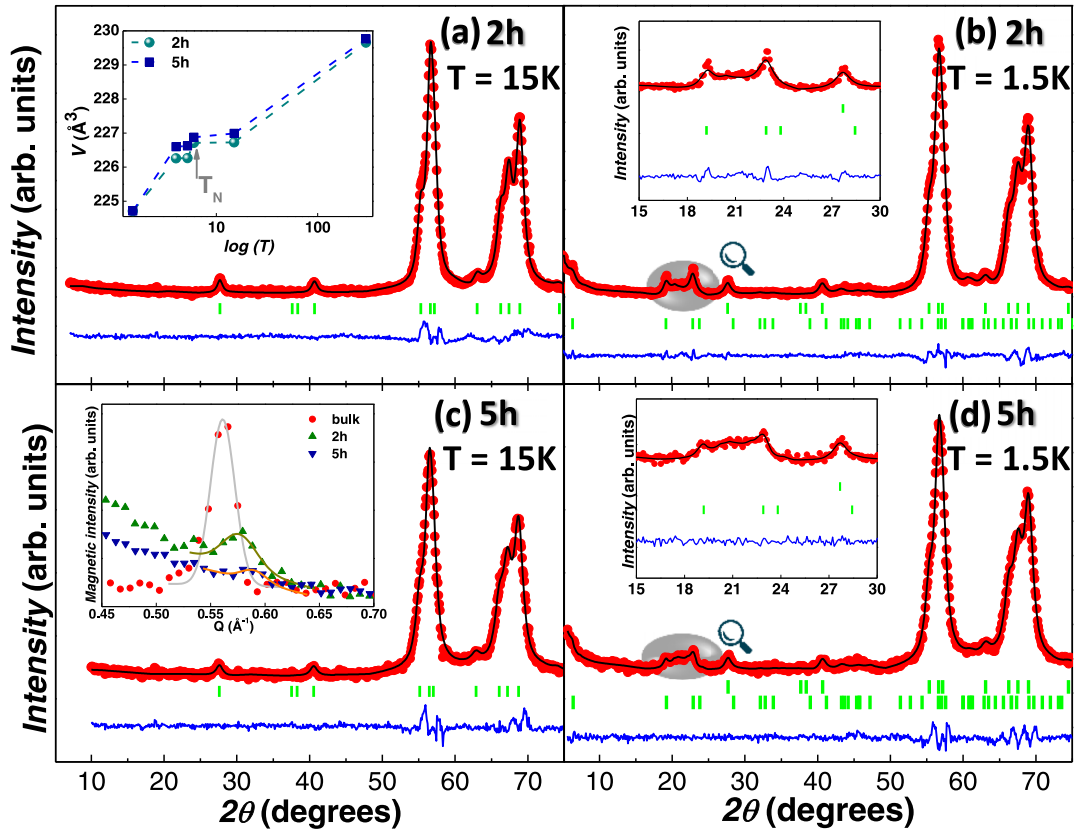

FIG. 1. Neutron diffraction patterns ($\lambda = 2.426$ Å) and Rietveld refinements for (a), (b) $NdCu_2$ 2 h-milled and (c), (d) 5 h-milled MNPs measured at (a), (c) $T = 15$ K and (b), (d) $T = 1.5$ K, which correspond to the PM and magnetic ordered regions, respectively. The inset in (a) shows the reduction of the unit cell volume with decreasing temperature. The position of the Néel transition is marked by the gray arrow. The inset in (c) shows the progressive disappearance of the magnetic peak located at $Q \approx 0.55$ Å^{-1} with size reduction. The insets in (b) and (d) allow us to observe in closer detail the broadening of the magnetic reflection within the range $18.5^\circ < 2\theta < 24^\circ$.

$\langle D_N \rangle = 16.5(4)$ nm ($R_B = 2.4\%$), whereas the magnetic one is $\langle D_m \rangle = 15.5(3)$ nm ($R_B = 6.64\%$) for 2 h-milled MNPs. 5 h-milled MNPs display $\langle D_N \rangle = 12.6(6)$ nm ($R_B = 1.56\%$) and $\langle D_m \rangle = 12.4(3)$ nm ($R_B = 4.7\%$). The fact that $\langle D_m \rangle$ is always close to but slightly smaller than $\langle D_N \rangle$ is due to the presence of a disordered moment arrangement, which is connected to the existence of interfaces. The rise in the magnetic scattering intensity observed in the low-Q region ($2^\circ < 2\theta < 15^\circ$, i.e., $Q < 0.665$ Å^{-1}, [see inset of Fig. 1(c)]) is indicative for interparticle correlations, which are triggered by dipolar interactions among MNPs [17,36]. The reduction in the AFM-coupled magnetic moments with size reduction is also supported by the gradual removal of the intense bulk magnetic peak located at $Q \approx 0.55$ Å^{-1}, i.e., $2\theta \approx 12.4^\circ$, as this peak gets progressively broadened and displaced to higher Q values with the size reduction.

The magnetic structure of the MNP cores can be fitted according to a commensurate square-up modulation in the same way as polycrystalline bulk $NdCu_2$ [46]. Each magnetic moment, which is oriented along the b direction, is ferromagnetically aligned in the b–c plane, and separated by $a/2$ with respect to each other. The propagation vectors are $\tau = (6/10, 0, 0)$ and the harmonic associated with 3τ. Given that Nd^{3+} ions are $J = 9/2$, i.e., Kramers type, a modulation in the intensity is expected [47]. To account for this modulation, we have employed the following Fourier series: $\mu = \mu_\tau \, sin(2\pi\tau R_i/a + \phi_1) + \mu_{3\tau} \sin(6\pi\tau R_i/a + \phi_3)$, where $R_i = 0, a/2, a, ..., 5a$ (sine-wave modulation), which results in magnetic moments of $\mu_\tau = 2.76(6)\ \mu_B$ (2 h MNPs) and $\mu_\tau = 2.64(6)\ \mu_B$ (5 h MNPs) associated with the first harmonic and $\mu_{3\tau} = 0.94(3)\ \mu_B$ and $\mu_{3\tau} = 0.98(3)\ \mu_B$ with the third $3\tau = (0.2, 0, 0)$ ($R_B = 10.7\%$ for 2 h MNPs and $R_B = 6.7\%$ for 5 h MNPs). These values give $M_0 = \pi/4 \times \mu_\tau = 2.2(1)\ \mu_B$ and $M_0 = \pi/4 \times \mu_\tau = 2.0(5)\ \mu_B$ magnetic moments values for 2 h and 5 h MNPs, respectively, and are smaller than the maximum theoretical magnetic moment of 3.27 μ_B. This finding, which has also been observed previously in the bulk alloy [39], can be understood by CEF influence on the Nd^{3+} ions [48]. The decrease of the magnetic-moment value with the MNP size confirms the reduction of the AFM-coupled entities.

2. Magnetic characterization. Dynamic $\chi_{AC}(T, f)$

The magnetic character of the $NdCu_2$ MNPs needs to be defined. The static magnetic behavior is presented in the *static $M(T, \mu_0 H)$ characterization* section in Ref. [49]. The outcome of the analyses is the presence of a disorder state, which may coexist with AFM within the MNPs cores. To access

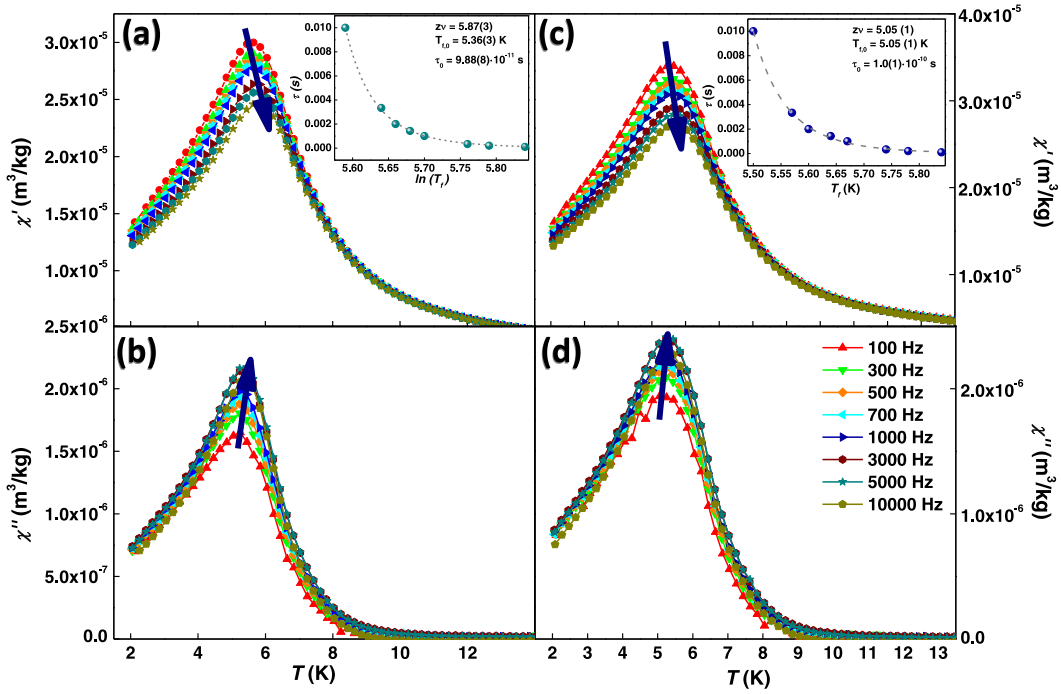

FIG. 2. In-phase $\chi'(T, f)$ [top panel, (a), (c)] and out–of–phase $\chi''(T, f)$ [bottom panel, (b), (d)] components of the dynamic susceptibility $\chi_{AC}(T, f)$, measured applying an oscillating field $h = 3.13$ Oe, for $t = 2$ h [left, (a), (b)] and $t = 5$ h [right, (c), (d)] $NdCu_2$ MNPs. The shift of the maximum associated with the SG state with the frequency of h is marked with dark blue arrows. Insets exhibit in closer detail the $\tau \equiv 1/(2\pi f)$ vs T_f dependence, where a scaling to a dynamical critical slowing down behavior (power law) is recovered, confirming the freezing (SG) nature of this transition. $\chi''(T, f)$ component displays dissipation associated with the SG state.

more information on this disorder state, dynamic susceptibility results are shown hereunder.

Dynamic susceptibility $\chi_{AC}(T, f)$ measurements corresponding to the in-phase $\chi'(T, f)$ (top panel) and out-of-phase $\chi''(T, f)$ components (bottom) are plotted in Fig. 2. Left-side panels [Figs. 2(a) and 2(b)] correspond to $NdCu_2$ 2 h-milled MNPs and right-side ones [Figs. 2(c) and 2(d)] to 5 h-milled ones. A maximum in $\chi'(T, f)$ occurs at around $T \approx 5.6$ K for 2 h and $T \approx 5.5$ K for 5 h-milled MNPs. This maximum, which is evidence of dissipation in $\chi''(T, f)$, reduces its value and shifts toward higher temperatures when increasing the frequency, which is a characteristic behavior of freezing transitions [18,50]. As the magnetic moments located within the core retain the bulk AFM state (see appear ND results included in the "structural characterization" section), there are the magnetic moments located at the MNP surface—the ones responsible for this SG-like state. In addition to this SG cusp, a maximum in $\chi'(T, f)$ corresponding to the AFM Néel transition should be observed at $T = T_N$. The fact that we only observe one single broad peak in $\chi'(T, f)$ is a consequence of the proximity of both T_N and T_f values.

To obtain more information about the freezing dynamics, we have analyzed the frequency dependence by determining both δ-shift parameter, $\delta = \ln T_f / \log_{10}(2\pi f) + k$, and the critical slowing down law $(\frac{T - T_{f,0}}{T_{f,0}})^{-z\nu}$, as is common practice [50–52]. First, δ-shift parameter values are 0.0218(7) for 2 h and 0.0301(3) for 5 h-milled MNPs, respectively. These values are larger with respect to the ones reported for canonical SGs [50], which is not surprising for MNP ensembles, where the concentration of magnetic ions is larger. Nevertheless, the obtained δ-shift parameter values are still below the upper limit of Superparamagnetic ensembles [53], which allow us to ensure the SG nature underlying the freezing dynamics of $NdCu_2$. These values are smaller than the ones corresponding to SAFM $TbCu_2$ [34] or SAFM $Tb_{0.5}La_{0.5}Cu_2$ MNPs [17], which suggests a more interacting SG ensemble in $NdCu_2$ MNPs. Second, the f shift of the T_f values scales up with the aforementioned dynamic critical slowing down law [see insets in Figs. 2 (a) and 2(c)]. Fitting parameters of $T_{f,0} = 5.36(3)$ K, $\tau_0 = 9.88(8) \times 10^{-11}$ s and $z\nu = 5.87(3)$ for 2 h-milled MNPs and $T_{f,0} = 5.05(1)$ K, $\tau_0 = 1.0(1) \times 10^{-10}$s and $z\nu = 5.05(1)$ for 5 h ones are obtained. These values are close to the ones reported for $Tb_{0.5}La_{0.5}Cu_2$ SAFM MNP ensembles [17,34] and lie within the expected range for SG freezing transitions [54]. Finally, given the slight increase of δ-shift parameter, τ_0 and $z\nu$, together with the slight decrease of the $T_{f,0}$ as the MNPs get smaller, a decrease in the interaction among the magnetic moments with the size reduction can be stated. This finding has already been observed for SAFM $GdCu_2$ MNPs [35], where it has been shown how the disappearance of the AFM RKKY interactions harms the interactions among the magnetically disordered moments, resulting in a weakened SG state. It may be possible that, if a further reduction of mean size in the NPs is studied (via an increased milling time), the magnetic structure might result in an overall SG state, as discussed in detail in Ref. [35]. Finally, no trace for the bulk reorientation temperature ($T_R \sim 4.5$ K) is found at the NP state. Bearing in mind both ND and magnetic measurements,

a SAFM state should be then ascribed for $t = 2$ h and $t = 5$ h milled MNPs.

3. Specific-heat measurements

Heat capacity measurements are a useful tool that provide an initial guide to unveil the magnetic excitations. Following common practice [39,55,56], the specific heat c_P has been assumed to be formed by the sum of a phononic c_{ph}, electronic c_{el} and magnetic c_{mag} contributions, as

$$c_P = c_{ph} + c_{el} + c_{mag}. \quad (1)$$

The former two contributions are usually grouped in a single term, $c_{lattice}$. Given that there exist two different local coordination and symmetry environments within the MNPs, here we propose a more subtle analysis, where we have calculated two different $c_{lattice}$ contributions, one that accounts for the MNP core and a second one that is responsible for the MNP surface, where the reduced symmetry and enhanced distortion soften the phonon modes [17,57]. Both contributions have been weighted, as $\approx 30\%$ of the magnetic moments are located within the MNP core for a $\langle D \rangle \approx 13$ nm, assuming a 2-nm-thickness shell (see the Estimating the Core-to-Volume Ratio section in Ref. [58]). This value for the shell thickness has been chosen based on several studies performed on diverse ensembles of MNPs, where the surface thickness has been found to be around ~ 2 nm [36,59,60]. Accordingly, the $c_{lattice}$ contribution has been fitted following

$$c_{lattice} = N_c\left[\gamma_c T + 9R\left(\frac{T}{\theta_D^c}\right)\int_0^{\theta_D^c/T} dx \frac{x^4 e^x}{(e^x-1)^2}\right] + N_s\left[\gamma_s T + 9R\left(\frac{T}{\theta_D^s}\right)\int_0^{\theta_D^s/T} dx \frac{x^4 e^x}{(e^x-1)^2}\right], \quad (2)$$

where a differentiation between the core and the surface is made. Accordingly, the values for γ^{core} and θ^{core} have been obtained from the analysis of the c_P of the bulk alloy, as the magnetic results point to a bulklike behavior of the magnetic core moments. In this way, we obtain $\gamma^{core} = 12.14(13)$ mJ(molK^2)$^{-1}$ and $\theta_D^{core} = 224.7(6)$ K, values that are in good agreement with the ones reported in Ref. [39]. On the other hand, we have obtained $\gamma^{surface} = 22.82(2)$ mJ/(molK^2)$^{-1}$ and $\theta_D^{surface} = 281(4)$ K. These fittings are shown in the right inset of Fig. 3, inserted in to the right pannel.

The c_{mag} contribution is then obtained following Eq. (1) by simply subtracting $c_{lattice}$ from the experimental c_P. Figure 3 shows the resulting c_{mag} (blue spheres), together with the contribution to the specific heat arising from the CEF, c_{CEF} (pink line), which has been calculated as

$$c_{CEF} = \frac{1}{kT^2}\left[\sum_i E_i^2 p_i - \left(\sum_i E_i p_i\right)^2\right], \quad (3)$$

with $p_i = \frac{e^{-E_i/kT}}{\sum_j e^{-E_j/kT}}$ being the Boltzmann factor. It should be kept in mind that this contribution accounts for the CEF, thus, it does not include the λ anomaly arising from the magnetic part.

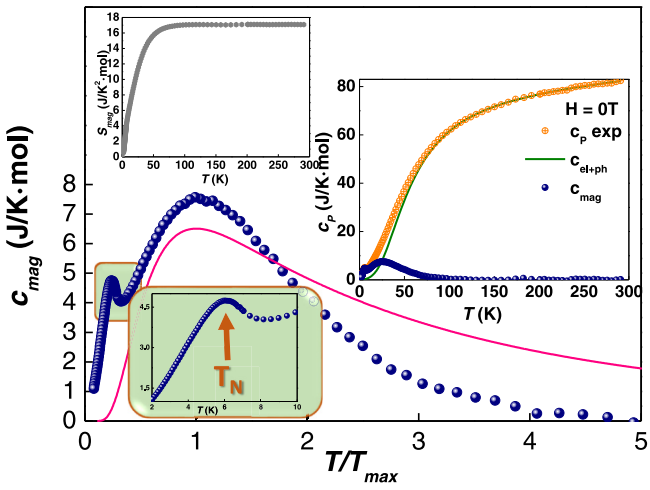

FIG. 3. Magnetic specific heat of $NdCu_2$–5 h milled MNPs, where the AFM λ anomaly is found at $T \sim 6$ K (zoomed in green–bottom inset). This c_{mag} contribution has been obtained by subtracting the $c_{lattice}$ contribution to the measured c_P (right inset). The pink line corresponds to the calculated contribution arising from the CEF, c_{CEF}. Left top inset corresponds to the $S_{mag}(T)$ dependence, where a maximum value of $S_{mag}^{exp} = 17.1$ (1) J/mol×K^2 is obtained.

Beginning from the low-temperature region, it is worth noting how the λ anomaly (zoomed in, the green-shadowed bottom inset), associated with the core AFM state, remains at the same $T_N = 6.2(1)$ K than the bulk one. Interestingly, no trace for the moment reorientation is observed at $T_R \sim 4.5$ K, which supports the idea of the weakening of the AFM coupling in the MNPs. The reduction of the c_{mag} value at T_N in the MNP state further backs this enfeeblement.

Above T_N, a broad peak, located between 10 K $\lesssim T \lesssim$ 80 K is found. This peak, that corresponds to the Schottky anomaly, is caused by the splitting of the energy levels driven by the CEF. This finding is of fundamental interest to the interpretation of collective excitations, as it could be indicating that the CEF-level schemes remain almost unaltered in spite of the size reduction and the microstrain of the MNPs. If we compare the experimental c_{mag} with the calculated c_{CEF}, it can be seen that the temperature value at which the maximum Schottky contribution is found shifts up to higher temperatures for the experimental data, as $T_{exp} - T_{calc} \approx 8$ K. This mismatch between the experimental and the calculated contributions to the specific heat was also detected for the bulk parent alloy, being indicative of the existence of temperature-dependent interactions, such as magnetoelastic effect and/or short-range correlations among Nd^{3+}, also reported in Ref. [39]. To access more information, we have removed these temperature-dependent interactions by normalizing both experimental and calculated contributions to their respective temperature value for which the Schottky anomaly is maximum (T/T_{max}) (see Fig. 3). The measured c_{mag} falls to zero above the Schottky anomaly faster than expected according to the calculated

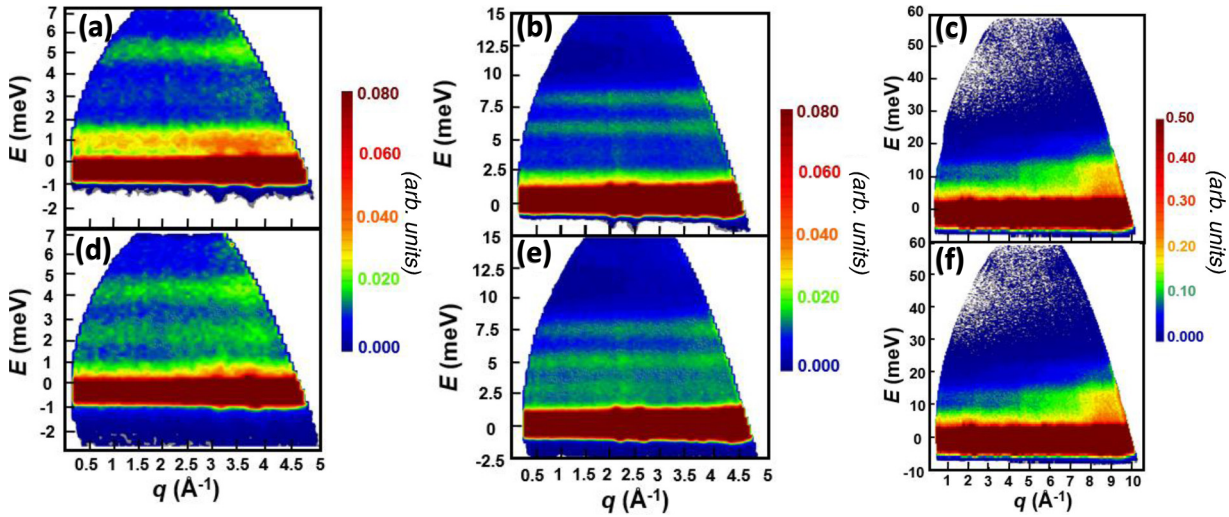

FIG. 4. Contour plots of the scattering function $S(Q, \hbar\omega)$ as a function of wave vector and energy of 13 nm $NdCu_2$ nanoparticles measured at $T = 1.5$ K in the magnetically ordered phase (top) and at $T = 10$ K in the paramagnetic phase (bottom) for incoming neutron energies of $E_0 = 8.8$, 16.7, and 66.7 meV (left to right).

c_{CEF} (pink line). This indicates that the CEF $|9/2\rangle$ multiplet is poorly defined, as its contribution to the specific heat is smooth. This macroscopic insight of the CEF schemes agrees well with the INS results (see below). The possible c_{mag} contribution stemming from the SG-coupled moments is too small compared to the one triggered by the CEF (see, for instance, Ref. [48], where the canonical CuMn SG gives a c_{mag} contribution that is 20% of the one calculated for the $NdCu_2$ c_{CEF}).

The dependence of the magnetic entropy S_{mag} with the temperature (Fig. 3, top inset) shows that the theoretical value $S_{\mathrm{mag}}^{\mathrm{theo}}$ (300 K) $= R[\ln(2J+1)] = 19.14$ J/mol×K^2 is not reached, as $S_{\mathrm{mag}}^{\mathrm{exp}} = 17.1(1)$ J/mol×K^2. The $S_{\mathrm{mag}}^{\mathrm{exp}}$ is also reduced with respect to the bulk alloy value of $S_{\mathrm{mag}}^{\mathrm{exp}} = 18.9$ (1) J/mol×K^2 (not shown), which is explained by the decrease of the AFM-coupled magnetic moments. The fact that four out of five energy levels are populated at $T \sim 70$ K leads the S_{mag} to reach 90% of its maximum value already at this temperature. In the vicinity of T_N, $S_{\mathrm{mag}}^{\mathrm{exp}} \approx 3.85(1)$ J/mol×K^2, which is also below the expected value $S_{\mathrm{mag}}^{\mathrm{exp}}(T_{\mathrm{N}}) = R[\ln(2)] = 5.76$ J/mol ×K^2 for a completely removal of the twofold moment degeneracy of the CEF ground-state doublet. Short-range correlations effects, already argued in polycrystalline $NdCu_2$ [39] or $CeCu_2$ [61], are at the origin of this finding.

All in all, the c_{P} analyses provide initial insight to the CEF schemes of the $NdCu_2$ MNPs, and the, the presence of the CEF energy-level scheme can be anticipated, in spite of the size reduction and the microstrain of the MNPs.

B. Inelastic neutron scattering

The scattering function $S(Q, \hbar\omega)$ for the 5 h-milled $NdCu_2$ MNPs is shown in Fig. 4 as a function of wave vector Q and energy transfer $\hbar\omega$. In the PM state at $T = 10$ K, the excitations corresponding to energy transfer from the ground state to the four excited levels can be distinctly seen for all measured temperatures in the contours of the scattering function $S(Q, \hbar\omega)$ [see Figs. 4(d)–4(f)]. The data collected at the higher incident energy $E_0 = 66.7$ meV [Figs. 4(c) and 4(f)] show that the total splitting ∼13.5 meV is lower than that of bulk $NdCu_2$, ∼14.1 meV. Spectra collected at lower incident energies of 8.8 and 16.7 meV show the different dispersionless excitations from the ground state to the first three excited CEF levels (∼2.8, ∼5.0, and ∼7.3 meV). These levels are the same as in bulk $NdCu_2$ within experimental precision [39].

In the magnetic state, at $T = 1.5$ K [Figs. 4(a)–4(c)], the CEF excitations at low energies (<3 meV) are strongly modified by the magnetic ordering and the exchange interactions, leading to a dispersive propagating transverse magnetic excitation [39,62–64], which is seen as a substantially broadened peak due to the powder averaging in our polycrystalline samples. The CEF levels that lie at 4.7 and 7.3 meV in the paramagnetic phase move up in energy to 5.7 and 7.8 meV, respectively, while higher lying levels are essentially unaffected by the magnetic order.

1. *CEF-level schemes for $NdCu_2$*

In $NdCu_2$, the Nd^{3+} ions are located at Wyckoff position $4e$ with point-group symmetry C_{2v} and the crystal electric field splits the tenfold degenerate Hund's rule ground-state multiplet $^4I_{9/2}$ of the Nd^{3+} ions with total angular momentum $J = 9/2$ into five doublets. The next multiplet state is located several hundreds of meV higher in energy [65]. The CEF and exchange Hamiltonian of C_{2v} symmetry takes the form

$$\mathcal{H} = \sum_i \sum_{\ell,m} B_\ell^m O_\ell^m(i) - \frac{1}{2} \sum_{ij} \mathcal{J}_{ij} \mathbf{J}_i \mathbf{J}_j, \qquad (4)$$

where the first term contains the CEF single-ion contributions involving the terms $\ell = 2, 4, 6$ and $m = 0, 2, 4$ and 6 with $m \leqslant \ell$, where O_l^m and B_l^m are the Stevens operators and CEF parameters, respectively [66]. The second term in Eq. (4) is related to the isotropic RKKY exchange interaction, where $\mathcal{J}_{ij}$ are the exchange coupling parameters and $\mathbf{J}_i$ the total angular momentum operator associated with the Nd^{3+} ion

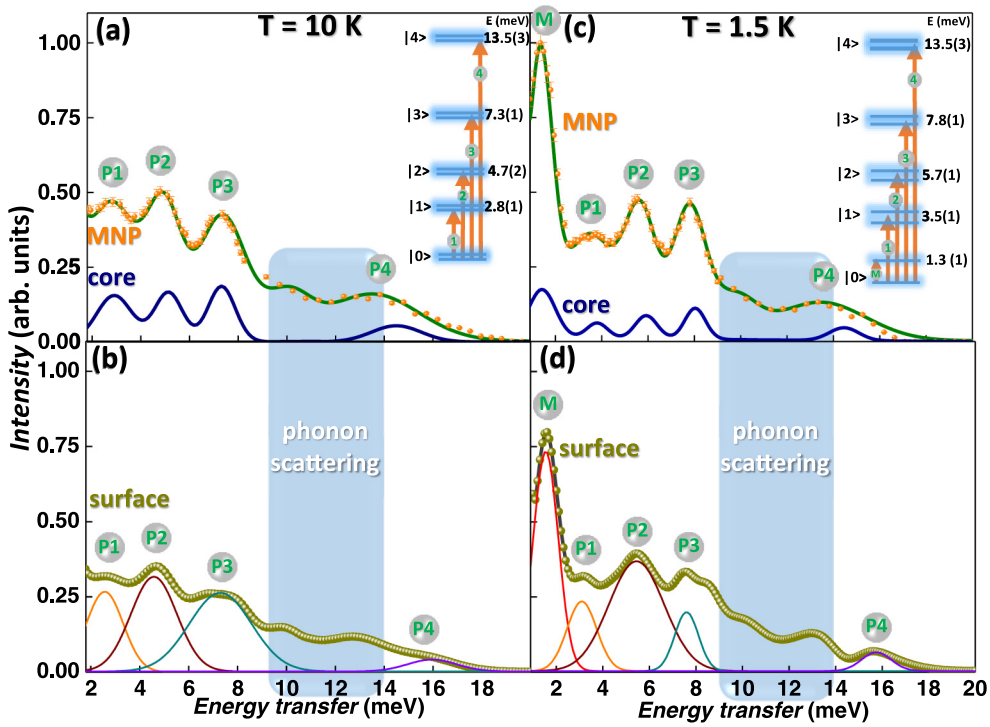

FIG. 5. (a), (c) $S(Q, \hbar\omega)$ of 5 h-milled $NdCu_2$ MNPs as a function of energy transfer for a wave vector of $Q = 1.75 \pm 0.5$ Å^{-1} (black symbols) at $T = 10$ K (left) and 1.5 K (right), obtained by combining data sets taken at different incoming energies. Error bars for the experimental MNP data are around 3%. Blue lines: Core contribution calculated from bulk $NdCu_2$ (see text). (b), (d) Surface contribution according to Eq. (7). Thin lines show fits of Gaussians to the data. The blue rectangle ranging from 9 to 14 meV indicates the region where phonon scattering is masking the magnetic signal (see Ref. [75]). The insets in (a) and (c) show the CEF-level schemes in the paramagnetic and magnetically ordered phases, respectively, where the blue blurred regions around each level represent the distribution of energies.

located on site i. The magnetic dipole-dipole interactions are not considered.

The CEF and exchange parameters in Eq. (4) were determined from a joint analysis of specific heat, magnetization, magnetic susceptibility, and INS measurements above T_N [39,62–64]. These results suggest a doublet CEF ground state formed by $|0\rangle = 0.049\,|\pm 9/2\rangle + 0.891\,|\mp 7/2\rangle - 0.373\,|\pm 5/2\rangle - 0.230\,|\mp 3/2\rangle + 0.111\,|\pm 1/2\rangle$ in the basis $|J, M_J\rangle \equiv |M_J\rangle$, which is responsible for the uniaxial orthorhombic easy-axis single-ion anisotropy. The first excited state is $|1\rangle = \mp 0.025\,|\pm 9/2\rangle \pm 0.309\,|\mp 7/2\rangle \pm 0.306\,|\pm 5/2\rangle \pm 0.284\,|\mp 3/2\rangle \mp 0.854\,|\pm 1/2\rangle$ located at an energy of 2.9 meV and the second excited level is $|2\rangle = -0.010\,|\pm 9/2\rangle + 0.120\,|\mp 7/2\rangle + 0.724\,|\pm 5/2\rangle - 0.675\,|\mp 3/2\rangle + 0.079\,|\pm 1/2\rangle$ at 5.0 meV [39]. The remaining two $J = 9/2$ levels lie at higher energies [see Figs. 4(a)–4(f)]. The latter are retained in the model calculations but are of no relevance for the low–energy magnetic excitations studied in this work or the ground-state properties [39].

Similar to the paradigmatic case of $PrNi_2Si_2$ [67–70], we have used a numerical procedure to calculate the magnetic excitations in the ordered phase within the random phase approximation (RPA), where we treat Eq. (4) in the mean-field approximation [71,72]. As commented above in Sec. III A 1, the magnetic periodicity is taken into account using a long-period commensurate propagation vector, $\boldsymbol{\tau} = (6/10, 0, 0) \equiv (0.6, 0, 0.0)$. This means that the magnetic unit cell is assumed to be ten times the length of the body-centered orthorhombic unit cell, corresponding to a period of 20 atomic Nd^{3+} layers along the a axis.

2. *Neutron scattering intensity at the nanoparticle surface*

The neutron-scattering intensity is given by

$$S(\mathbf{Q}, \hbar\omega) = -\frac{1}{\pi}\frac{1}{1 - \exp(-\hbar\omega/k_B T)}\,|f(\mathbf{Q})|^2 \times \sum_{\alpha\beta}\left(\delta_{\alpha\beta} - \frac{Q_\alpha Q_\beta}{|\mathbf{Q}|^2}\right)\mathrm{Im}\{G^{\alpha\beta}_{n=0}(\mathbf{Q}, \hbar\omega)\}, \quad (5)$$

where Q_α are the Cartesian components of the neutron-scattering vector $\mathbf{Q}$, and $f(\mathbf{Q})$ is the magnetic form factor of the Nd^{3+} ions. Since the magnetic unit cell has 20 nonequivalent sites, $n = 0, \ldots, 19$, the corresponding Fourier–transformed two-site Green's functions are coupled within the RPA theory through [71,73]

$$\overline{\overline{G}}_{\mathrm{N}}(\mathbf{q}, \hbar\omega) = \overline{\overline{g}}_{\mathrm{N}}(\hbar\omega) - \sum_{s=0}^{19}\overline{\overline{g}}_{n-s}(\hbar\omega)\overline{\overline{\mathcal{J}}}(\mathbf{q} + s\,\boldsymbol{\tau})\overline{\overline{G}}_s(\mathbf{q}, \hbar\omega), \quad (6)$$

where $\mathbf{q}$ is the reduced wave vector and $\overline{\overline{g}}_{\mathrm{N}}(\hbar\omega)$ is the nth Fourier component of the single-site dynamic magnetic susceptibility with negative sign calculated from the mean-field levels of the magnetic system shown in Fig. 5. The 20 equations of 3×3 matrices in Eq. (6) are solved

numerically after the introduction of a small imaginary energy width ϵ. The positions of the poles or the excitation energies have also been determined directly using the dynamical matrix diagonalization method implemented in the McPhase software package [74]. This calculation is used to determine the neutron-scattering intensity $S_c(\mathbf{Q}, \hbar\omega)$ of the Nd^{3+} magnetic moments associated with the core magnetic moments of the MNPs (see below).

Figures 5(a) and 5(b) show $S(Q, \hbar\omega)$ as a function of energy transfer for a wave vector of $Q = 1.75 \pm 0.5$ Å^{-1} at $T = 10$ and 1.5 K, respectively, obtained by combining data sets taken at different incoming energies. To isolate the surface contribution to the total scattering, we have considered the scattering from the MNP state to be a result of the sum of two distinct crystallographic environments, i.e., the NP core and its surface. Bearing in mind the preliminary characterization shown earlier in this paper, we have assumed the magnetic moments located within the core to behave in a way similar to the bulk [38]. The results on the crystalline and magnetic microstructure provided by ND, together with the magnetic characterization, especially, $\chi_{AC}(T, f)$ dynamic scaling, are unambiguous to this respect. Furthermore, the conservation of the bulk nature at the MNP core was also reported for other RCu_2 MNPs [17,35,36]. Given this fact, we can then extract the surface contribution to the INS, $S_{surface}(Q, \hbar\omega)$, as

$$S_{surface}(Q, \hbar\omega) = S(Q, \hbar\omega) - N\, S_{core}(Q, \hbar\omega), \qquad (7)$$

where the core contribution $S_{core}(Q, \hbar\omega)$ is calculated using the known crystalline-electric-field parameters from the bulk, and N is a factor that weights the fraction of atoms located within the MNP core. According to the MNP size ($\langle D\rangle \approx$ 13 nm), simple approximations lead to $N \approx 0.3$, as the core represents ≈30% of the MNP volume (see the Estimating the Core-to-Volume Ratio section in Ref. [58]).

The resulting $S_{surface}(Q, \hbar\omega)$ is shown in Figs. 5(b) (T =10 K, PM state) and 5(d) (T = 1.5 K, SAFM state). There, both CEF (P1–P4) and collective magnetic excitations can be clearly observed. This is stunning, as it indicates that the bulk CEF energy-level schemes and magnon excitations are well preserved even at the surface of the MNPs. At this stage, it is worth emphasizing that, although we have tried different N values to account for this surface $S_{surface}(Q, \hbar\omega)$ (see the Isolating the Surface Contribution from the Total MNP INS Intensity section in Ref. [75]), these collective excitations do not disappear for any of the chosen values. Hence, it is reasonable to keep $N = 0.3$ as it is, according to the aforementioned estimations, the most likely core/MNP ratio for $\langle D\rangle \approx 13$ nm.

Quantitative information can be obtained by inspecting in closer detail both $S_{surface}(Q, \hbar\omega)$ contributions. First, concerning the PM phase [$T = 10$ K, Fig. 5(b)], a left–shift of the energy transfer values can be determined for transitions from the ground state to the first and second excited levels. In this way, CEF excitations are found at $\hbar\omega_{P1} = 2.6$ and $\hbar\omega_{P2}$ =4.6 meV for the MNP surface, whereas they were found at $\hbar\omega_{P1} = 2.9$ and $\hbar\omega_{P2}$ =5.0 meV for the bulk state [38]. This fact reveals a softening of the CEF splitting, which can be ascribed to the less symmetric crystalline environment in the proximity of the MNP interfaces. This softening may also affect the higher energy excitations (P3 and P4). Nevertheless, the presence of phonon scattering makes it difficult to precisely determine their energy transfer values. Particularly, this scattering becomes rather strong in the energy range from 9 to 14 meV (blue-shadowed region in Fig. 5), which makes the determination of the P4 position especially rough. This phonon scattering has been confirmed by measuring the INS in nonmagnetic isostructural YCu_2 MNPs (see the YCu_2-Phonon Contribution to INS Spectra section in Ref. [76]). Additionally, the poor definition of the $|9/2\rangle$ multiplet (i.e., P4 excitation) was already foreseen by the specific heat analyses.

On the other hand, change of the relative peak areas between P1 and P2 occurs at the MNP state [Figs. 5(a) and 5(b)]. In this way, whereas an almost homogeneous ratio between the peak areas $P2/P1$ was found in bulk $NdCu_2$ [39], the value $P2/P1$ is almost 30% decreased at both the surface and the whole MNP state. This reveals a partial inhibition of the transitions from the ground state to the first excited level, which reveals that the bulk local-symmetry environment is slightly distorted at the MNPs. The structural microstrain η is at the basis of this distortion. Even if minimal ($\eta < 1\%$), it slightly changes the cation distribution surrounding the Nd^{3+} ions, thus provoking the decoherence of some CEF excitations. Of course, this distortion should also affect P2–P4 transitions, but its effect is almost not noticeable within the experimental resolution, given that the distortion is very subtle ($\eta < 1\%$). Therefore, it can only be detected for the most intense excitation (i.e., from the ground state to the first excited level, P1). Given that this partial inhibition from the ground state to the first excited level is close but slightly greater at the whole MNP $S(Q, \hbar\omega)$ than the one at the $S_{surface}(Q, \hbar\omega)$, both the core and surface microstrains are definitely playing a role. Therefore, we can state that the intermediate regions between the AFM-ordered MNP cores and SG-disordered surfaces in MNPs play the same role as *interfaces* do in multilayers, where a modification of both CEF-level splittings and ground-state wave functions was reported (e.g., in Fe–Nd multilayers [26]).

Second, the magnetically ordered phase [T = 1.5 K, Fig. 5(d)] shows the coexistence of collective magnetic excitations and CEF levels, which is actually unprecedented, as the loss of periodicity at interfaces is well-known to affect the magnetic interactions. Here, the lowest energy excitation (peak labeled M) is found at $\hbar\omega \approx 1.6$ meV, whereas the bulk one appeared at $\hbar\omega \approx 1.4$ meV [39]. This represents a shift of ∼15%. Given the minor uncertainty associated with the measured energy transfer $\hbar\omega$ (∼3%), this shift can be considered unambiguous. The investigations carried out by Gratz *et al.* [39] on the bulk state related this peak to a transverse spin-wave mode generated from the AFM $NdCu_2$ ground state. This positive shift may be ascribed to an enhancement of the anisotropy constant, K, as has been shown, for instance, in Ref. [77]. In the case of our MNPs, this enhancement could be ascribed to both size effects and microstrain.

IV. DISCUSSION

We have been able to produce a large quantity (∼ 12 g) of $NdCu_2$ MNPs by the ball-milling route. Relatively low milling times (t = 5 h) have been enough to achieve 13 nm-sized MNPs in the same way as other RCu_2 MNPs [17,34–36]. The

produced MNPs retained the AFM bulk structure at the core and a disordered SG state for the magnetic moments sitting at the surface, which is also common for nano-RCu_2 or RAl_2 [17,34–36,78].

The experimental data (c_P, INS) have shown the occurrence of CEF and magnon collective excitations for the $NdCu_2$ 13-nm MNPs. Although the general picture shows that the level schemes remain very similar to the bulk situation, some subtle differences have been disclosed thanks to the evaluation of the surface contribution to the total INS, which has been obtained following Eq. (7). This allows us to access quantitative information regarding the CEF and magnon collective excitation propagation at the MNP surface. One point that should be addressed concerns the N value shown in Eq. (7). Although it has been estimated in a *simplified* manner (see the section Estimating the Core-to-Volume Ratio in Ref. [58]), the prevalence of collective excitations at the surface does not dependent on the different N values. To ensure this, we have considered a wide variety of N values (see some examples shown in the Isolating the Surface Contribution from the Total MNP INS Intensity section [76]) and both the CEF and magnon excitations did remain. In any case, this small uncertainty around the N value is not a hindrance to the main conclusions of this paper.

Regarding the surface INS contribution, the loss of long-range symmetry at the NP surface has revealed not to be enough to rule out the CEF level schemes. This fact reveals that the CEF is robust against local symmetry distortions. Second, it turns out that transitions to the first excited level at $T = 10$ K are partially inhibited with respect to the bulk landscape reported in Ref. [39]. This partial inhibition is deduced from the decrease in the intensity for transitions from the ground state to the first excited level, and can be attributed to a distortion of the local-symmetry environment surrounding each Nd^{3+}–ion. Nevertheless, it should be kept in mind that the distortion of the crystalline structure is below 1%, according to XRD (see Ref. [40]). Therefore, this effect is weak, i.e., it is only detected for the first excitation, which is the most intense one. It cannot be discarded, of course, that this distortion could be affecting the rest of the transitions, but as they are less intense, its effect is not noticeable within the experimental resolution. Further INS experiments using different resolutions and/or other MNP ensembles may be helpful to complete this statement.

At $T = 1.5$ K (magnetic state), a positive shift in the energy associated with the spin-wave excitations is found at the MNP state. The reason for this displacement ($\sim$ 15%) might be ascribed to the enhanced magnetic anisotropy at the NP state, which is supported by the $M(T, H)$ characterization (see the Static $M(T, H)$ Characterization section in Ref. [49]) . Although our experimental evidence is unambiguous, it holds true that this leaves an open path to further INS experiments to be performed, where different MNP sizes could be evaluated. We recall at this point that it is challenging to perform INS in MNP ensembles [19,20,32,33].

V. CONCLUSION

INS measurements on polycristalline $NdCu_2$ NPs of $\langle D \rangle \approx$ 13 nm size have been successfully carried out. We have extracted the surface contribution from the total scattering intensity, being able to experimentally observe that the CEF-level schemes, as well as magnon excitations, are well-defined at the MNP surface despite the distortion of these outer atoms. In this way, the reduction in the local coordination symmetry, as well as the structural distortion and magnetic disorder of the outer Nd^{3+} ions, do not significantly affect the CEF Hamiltonian. Nevertheless, the results and analyses presented in this paper have allowed us to deepen inside the subtleties concerning the propagation of collective excitations in the MNP state. In this way, it has been possible to determine a partial inhibition of the transitions from the ground state to the first excited level, as well as a slight positive shift ($\sim$15%) of the energy transfer corresponding to magnon excitations. Both effects can be ascribed to finite-size effects (local-symmetry coordination, dimensionality) and microstrain. The present INS observations in $NdCu_2$ pave the way for studies in which interfaces between geometrically ordered and disordered regions are present in nanocrystalline materials. In particular, it would be interesting to analyze the excitations at higher energy using similar ensembles of $4f$ NPs, as well as to disclose the energy shift of the magnon excitations using a neutron spectrometer with better energy resolution.

ACKNOWLEDGMENTS

This paper has been financially supported by Spain's Projects No. MCIU MAT2017–83631-C3–R and No. RTI2018-094683–B–C52 and Principado de Asturias Regional Government Project No. IDI/2018/000185. E.M.J. was supported by Beca Concepción Arenal No. BDNS: 406333 (Gobierno de Cantabria-U. Cantabria). M.R.F. was supported by FPI (BES–2012–058722). We acknowledge Laboratoire Léon Brillouin and Institut Laue–Langevin for allocation of beamtime and resources.

[1] R. Kodama, Magnetic nanoparticles, J. Magn. Magn. Mater. **200**, 359 (1999).

[2] A.-H. Lu, E. L. Salabas, and F. Schüth, Magnetic nanoparticles: synthesis, protection, functionalization, and application, Angew. Chem. Int. Ed. **46**, 1222 (2007).

[3] G. Reiss and A. Hütten, Applications beyond data storage, Nat. Mater. **4**, 725 (2005).

[4] A. Moser, K. Takano, D. T. Margulies, M. Albrecht, Y. Sonobe, Y. Ikeda, S. Sun, and E. E. Fullerton, Magnetic recording: advancing into the future, J. Phys. D: Appl. Phys. **35**, R157 (2002).

[5] L. Gloag, M. Mehdipour, D. Chen, R. D. Tilley, and J. J. Gooding, Advances in the application of magnetic nanoparticles for sensing, Adv. Mater. **31**, 1904385 (2019).

[6] Q. A. Pankhurst, J. Connolly, S. K. Jones, and J. Dobson, Applications of magnetic nanoparticles in biomedicine, J. Phys. D: Appl. Phys. **36**, R167 (2003).

[7] P. Guardia, A. Labarta, and X. Batlle, Tuning the size, the shape, and the magnetic properties of iron oxide nanoparticles, J. Phys. Chem. C **115**, 390 (2011).

[8] J. Nogués, J. Sort, V. Langlais, V. Skumryev, S. Suriñach, J. Muñoz, and M. Baró, Exchange bias in nanostructures, Phys. Rep. **422**, 65 (2005).

[9] I. Orue, L. Marcano, P. Bender, A. García-Prieto, S. Valencia, M. Mawass, D. Gil-Cartón, D. A. Venero, D. Honecker, A. García-Arribas *et al.*, Configuration of the magnetosome chain: A natural magnetic nanoarchitecture, Nanoscale **10**, 7407 (2018).

[10] X. Chen, S. Bedanta, O. Petracic, W. Kleemann, S. Sahoo, S. Cardoso, and P. P. Freitas, Superparamagnetism versus superspin glass behavior in dilute magnetic nanoparticle systems, Phys. Rev. B **72**, 214436 (2005).

[11] P. Bender, D. Honecker, and L. Fernández Barquín, Superferromagnetic correlations in clusters of magnetic nanoflowers, Appl. Phys. Lett. **115**, 132406 (2019).

[12] J. Alonso, M. L. Fdez-Gubieda, J. Barandiarán, A. Svalov, L. F. Barquín, D. A. Venero, and I. Orue, Crossover from superspin glass to superferromagnet in Fe_xAg_{100-x} nanostructured thin films ($20 \leqslant x \leqslant 50$), Phys. Rev. B **82**, 054406 (2010).

[13] H. Gleiter, Nanocrystalline materials, Prog. Mater. Sci. **33**, 223 (1989).

[14] S. Das, Y. Tang, Z. Hong, M. Gonçalves, M. McCarter, C. Klewe, K. Nguyen, F. Gómez-Ortiz, P. Shafer, E. Arenholz *et al.*, Observation of room-temperature polar skyrmions, Nature (London) **568**, 368 (2019).

[15] A. Brinkman, M. Huijben, M. Van Zalk, J. Huijben, U. Zeitler, J. Maan, W. G. van der Wiel, G. Rijnders, D. H. Blank, and H. Hilgenkamp, Magnetic effects at the interface between nonmagnetic oxides, Nat. Mater. **6**, 493 (2007).

[16] D. Zákutná, D. Nižňansky, L. C. Barnsley, E. Babcock, Z. Salhi, A. Feoktystov, D. Honecker, and S. Disch, Field Dependence of Magnetic Disorder in Nanoparticles, Phys. Rev. X **10**, 031019 (2020).

[17] E. M. Jefremovas, M. de la Fuente Rodríguez, J. Alonso, J. R. Fernández, J. Espeso, I. Puente-Orench, D. Rojas, A. García-Prieto, M. Fdez-Gubieda, L. R. Fernández, and L. Barquín, Exploring the different degrees of magnetic disorder in $Tb_xR_{1-x}Cu_2$ nanoparticle alloys, Nanomaterials **10**, 2148 (2020).

[18] G. F. Zhou and H. Bakker, Spin-Glass Behavior of Mechanically Milled Crystalline $GdAl_2$, Phys. Rev. Lett. **73**, 344 (1994).

[19] S. N. Klausen, K. Lefmann, P.-A. Lindgård, Theil Kuhn, C. R. H. Bahl, C. Frandsen, S. Mørup, B. Roessli, N. Cavadini, and C. Niedermayer, Magnetic anisotropy and quantized spin waves in hematite nanoparticles, Phys. Rev. B **70**, 214411 (2004).

[20] S. Disch, R. P. Hermann, E. Wetterskog, A. A. Podlesnyak, K. An, T. Hyeon, G. Salazar-Alvarez, L. Bergström, and T. Brückel, Spin excitations in cubic maghemite nanoparticles studied by time-of-flight neutron spectroscopy, Phys. Rev. B **89**, 064402 (2014).

[21] J. Robert, E. Lhotel, G. Remenyi, S. Sahling, I. Mirebeau, C. Decorse, B. Canals, and S. Petit, Spin dynamics in the presence of competing ferromagnetic and antiferromagnetic correlations in $Yb_2Ti_2O_7$, Phys. Rev. B **92**, 064425 (2015).

[22] M. Dabrowski, T. Nakano, D. M. Burn, A. Frisk, D. G. Newman, C. Klewe, Q. Li, M. Yang, P. Shafer, E. Arenholz *et al.*, Coherent Transfer of Spin Angular Momentum by Evanescent Spin Waves within Antiferromagnetic NiO, Phys. Rev. Lett. **124**, 217201 (2020).

[23] Y. Nambu, J. Barker, Y. Okino, T. Kikkawa, Y. Shiomi, M. Enderle, T. Weber, B. Winn, M. Graves-Brook, J. Tranquada *et al.*, Observation of Magnon Polarization, Phys. Rev. Lett. **125**, 027201 (2020).

[24] S. Philippi, J. Markmann, R. Birringer, and A. Michels, Grain-size-dependent magnetic susceptibility of nanocrystalline terbium, J. Appl. Phys. **105**, 07A701 (2009).

[25] P. Das, P.-F. Lory, R. Flint, T. Kong, T. Hiroto, S. L. Bud'ko, P. C. Canfield, M. de Boissieu, A. Kreyssig, and A. I. Goldman, Crystal electric field excitations in the quasicrystal approximant $TbCd_6$ studied by inelastic neutron scattering, Phys. Rev. B **95**, 054408 (2017).

[26] L. T. Baczewski, M. Piecuch, J. Durand, G. Marchal, and P. Delcroix, Influence of interface effects on a rare-earth crystal field in iron–rare-earth multilayers, Phys. Rev. B **40**, 11237 (1989).

[27] S. Mørup, M. B. Madsen, J. Franck, J. Villadsen, and C. J. Koch, A new interpretation of Mössbauer spectra of microcrystalline goethite:"super-ferromagnetism" or "super-spin-glass" behaviour? J. Magn. Magn. Mater. **40**, 163 (1983).

[28] S. Bedanta, T. Eimüller, W. Kleemann, J. Rhensius, F. Stromberg, E. Amaladass, S. Cardoso, and P. P. Freitas, Overcoming Thedipolar Disorder in Dense Cofe Nanoparticle Ensembles: Superferromagnetism, Phys. Rev. Lett. **98**, 176601 (2007).

[29] M. Hermele, M. P. A. Fisher, and L. Balents, Pyrochlore photons: The $U(1)$ spin liquid in a s= 1/2 three-dimensional frustrated magnet, Phys. Rev. B **69**, 064404 (2004).

[30] M. J. Gingras and P. A. McClarty, Quantum spin ice: a search for gapless quantum spin liquids in pyrochlore magnets, Rep. Prog. Phys. **77**, 056501 (2014).

[31] Y. Shen, Y.-D. Li, H. Wo, Y. Li, S. Shen, B. Pan, Q. Wang, H. Walker, P. Steffens, M. Boehm *et al.*, Evidence for a spinon fermi surface in a triangular-lattice quantum-spin-liquid candidate, Nature (London) **540**, 559 (2016).

[32] M. Hennion, C. Bellouard, I. Mirebeau, J. Dormann, and M. Nogues, Dual spin dynamics of small Fe particles, Europhys. Lett. **25**, 43 (1994).

[33] M. F. Hansen, F. Bødker, S. Mørup, K. Lefmann, K. N. Clausen, and P.-A. Lindgård, Dynamics of Magnetic Nanoparticles Studied by Neutron Scattering, Phys. Rev. Lett. **79**, 4910 (1997).

[34] C. Echevarria-Bonet, D. P. Rojas, J. I. Espeso, J. R. Fernández, M. de la Fuente Rodríguez, L. F. Barquín, L. R. Fernández, P. Gorria, J. A. Blanco, M. Fdez-Gubieda, E. Bauer, and F. Damay, Magnetic phase diagram of superantiferromagnetic $TbCu_2$ nanoparticles, J. Phys.: Condens. Matter **27**, 496002 (2015).

[35] E. Jefremovas, J. A. Masa, M. Rodríguez, J. R. Fernández, J. Espeso, D. Rojas, A. García-Prieto, M. Fernández-Gubieda, and L. F. Barquín, Investigating the size and microstrain influence in the magnetic order/disorder state of $GdCu_2$ nanoparticles, Nanomaterials **10**, 1117 (2020).

[36] C. Echevarria-Bonet, D. P. Rojas, J. I. Espeso, J. Rodriguez Fernández, L. Rodriguez Fernández, P. Gorria, J. A. Blanco, M. L. Fdez-Gubieda, E. Bauer, G. André, and L. Fernández Barquín, Size-induced superantiferromagnetism with reentrant spin-glass behavior in metallic nanoparticles of $TbCu_2$, Phys. Rev. B **87**, 180407(R) (2013).

[37] R. Bachmann, F. DiSalvo Jr, T. Geballe, R. Greene, R. Howard, C. King, H. Kirsch, K. Lee, R. Schwall, H.-U. Thomas *et al.*, Heat capacity measurements on small samples at low temperatures, Rev. Sci. Instrum. **43**, 205 (1972).

[38] M. Ellerby, K. McEwen, M. De Podesta, M. Rotter, and E. Gratz, Detailed magnetization study of $NdCu_2$ at low temperatures, J. Phys.: Condens. Matter **7**, 1897 (1995).

[39] E. Gratz, M. Loewenhaupt, M. Divis, W. Steiner, E. Bauer, N. Pillmayr, H. Muller, H. Nowotny, and B. Frick, Structural, magnetic, electronic and transport properties of $NdCu_2$, J. Phys.: Condens. Matter **3**, 9297 (1991).

[40] See Supplemental Material at http://link.aps.org/supplemental/10.1103/PhysRevB.104.134404 for additional information on x-ray fiffraction characterization, which includes Ref. [79].

[41] P. Thompson, D. Cox, and J. Hastings, Rietveld refinement of Debye-Scherrer synchrotron x-ray data from Al_2O_3, J Appl. Crystallogr **20**, 79 (1987).

[42] P. Morin and D. Schmitt, in *Quadrupolar Interactions and Magneto-Elastic Effects in Rare Earth Intermetallic Compounds* (Elsevier, London, 1990), Chap. 1.

[43] R. H. Kodama, S. A. Makhlouf, and A. E. Berkowitz, Finite Size Effects in Antiferromagnetic NiO Nanoparticles, Phys. Rev. Lett. **79**, 1393 (1997).

[44] N. Rinaldi-Montes, P. Gorria, D. Martínez-Blanco, A. Fuertes, L. F. Barquín, J. R. Fernández, I. de Pedro, M. Fdez-Gubieda, J. Alonso, L. Olivi *et al.*, Interplay between microstructure and magnetism in NiO nanoparticles: Breakdown of the antiferromagnetic order, Nanoscale **6**, 457 (2014).

[45] A. A. Baker, J. R. Lee, C. A. Orme, T. van Buuren, and S. K. McCall, Suppression of low temperature magnetic ordering in samarium nanoparticles, J. Phys.: Condens. Matter **32**, 495803 (2020).

[46] R. Arons, M. Loewenhaupt, T. Reif, and E. Gratz, The magnetic structures of $NdCu_2$ in zero field, J. Phys.: Condens. Matter **6**, 6789 (1994).

[47] T. Chatterji, in *Neutron Scattering From Magnetic Materials* (Elsevier, London, 2005), Chap. 6.

[48] L. Bozukov, A. Gilewski, E. Gratz, A. Apostolov, and K. Kamenov, High field magnetization and magneto-resistance of $NdCu_2$, Physica B: Condens. Matter **177**, 299 (1992).

[49] See Supplemental Material at http://link.aps.org/supplemental/10.1103/PhysRevB.104.134404 for additional information on static m_{DC} characterization, which includes Refs. [80–83].

[50] J. A. Mydosh, in *Spin Glasses: An Experimental Introduction* (Taylor and Francis, London, 1993), Chap. 4.

[51] P. Jönsson, M. Hansen, P. Svedlindh, and P. Nordblad, Spin-glass-like transition in a highly concentrated Fe-C nanoparticle system, J. Magn. Magn. Mater. **226**, 1315 (2001).

[52] Z. Fu, Y. Zheng, Y. Xiao, S. Bedanta, A. Senyshyn, G. G. Simeoni, Y. Su, U. Rücker, P. Kögerler, and T. Brückel, Coexistence of magnetic order and spin-glass-like phase in the pyrochlore antiferromagnet $Na_3Co(CO_3)_2Cl$, Phys. Rev. B **87**, 214406 (2013).

[53] S. Bedanta and W. Kleemann, Topical review superparamagnetism, J. Phys. D: Appl. Phys. **42**, 013001 (2009).

[54] J. Souletie and J. L. Tholence, Critical slowing down in spin glasses and other glasses: Fulcher versus power law, Phys. Rev. B **32**, 516 (1985).

[55] M. Bouvier, P. Lethuillier, and D. Schmitt, Specific heat in some gadolinium compounds. I. Experimental, Phys. Rev. B **43**, 13137 (1991).

[56] N. H. Luong, J. Franse, and T. D. Hien, Specific heat and thermal expansion in $Gd_xY_{1-x}Cu_2$, J. Phys. F: Metal Phys. **15**, 1751 (1985).

[57] D. Rojas, L. F. Barquín, J. R. Fernández, L. R. Fernández, and J. Gonzalez, Phonon softening on the specific heat of nanocrystalline metals, Nanotechnology **21**, 445702 (2010).

[58] See Supplemental Material at http://link.aps.org/supplemental/10.1103/PhysRevB.104.134404 for sketch and approximations.

[59] L. Del Bianco, D. Fiorani, A. M. Testa, E. Bonetti, L. Savini, and S. Signoretti, Magnetothermal behavior of a nanoscale Fe/Fe oxide granular system, Phys. Rev. B **66**, 174418 (2002).

[60] Q. A. Pankhurst, Á. Y. Martínez, and L. F. Barquín, Interfacial exchange pinning in amorphous iron-boron nanoparticles, Phys. Rev. B **69**, 212401 (2004).

[61] E. Gratz, N. Pillmayr, E. Bauer, H. Muller, B. Barbara, and M. Loewenhaupt, Low-temperature x-ray diffraction, transport properties, specific-heat, thermal expansion and magnetic investigations of $SmCu_2$, J. Phys.: Condens. Matter **2**, 1485 (1990).

[62] M. Loewenhaupt, T. Reif, W. Hahn, and B. Frick, Magnetic excitation spectra of $NdCu_2$, J. Magn. Magn. Mater. **177-181**, 1050 (1998).

[63] M. Rotter, M. Loewenhaupt, S. Kramp, T. Reif, N. M. Pyka, W. Schmidt, and R. van de Kamp, Anisotropic magnetic exchange in orthorhombic RCu_2 compounds (R=rare earth), Eur. Phys. J. B **14**, 29 (2000).

[64] M. Rotter, S. Kramp, M. Loewenhaupt, E. Gratz, W. Schmidt, N. M. Pyka, B. Hennion, and R. van de Kamp, Magnetic excitations in the antiferromagnetic phase $NdCu_2$ compound), Appl. Phys. A **74**, S751 (2002).

[65] J. H. van Vleck, in *The Theory of Electric and Magnetic Susceptibilities* (Oxford University Press, London, 1932), Chap. 9.

[66] M. T. Hutchings, Solid State Phys. **16**, 227 (1964).

[67] J. A. Blanco, D. Gignoux, and D. Schmitt, Phys. Rev. B **45**, 2529 (1992).

[68] J. A. Blanco, D. Schmitt, and J. C. Gómez-Sal, J. Magn. Magn. Mater. **116**, 128 (1992).

[69] J. A. Blanco, B. Fåk, E. Ressouche, B. Grenier, M. Rotter, D. Schmitt, J. A. Rodríguez-Velamazán, J. A. Campo, and P. Lejay, Phys. Rev. B **82**, 054414 (2010).

[70] J. A. Blanco, B. Fåk, J. Jensen, M. Rotter, A. Hiess, D. Schmitt, and P. Lejay, Phys. Rev. B **87**, 104411 (2013).

[71] K. A. McEwen, U. Steigenberger, and J. Jensen, Phys. Rev. B **43**, 3298 (1991).

[72] R. M. Nicklow and N. Wakabayashi, Phys. Rev. B **51**, 12425 (1995).

[73] J. Jensen and A. R. Mackintosh, in *Rare Earth Magnetism: Structures and Excitations* (Oxford University Press, Oxford, 1991).

[74] M. Rotter, M. D. Le, A. T. Boothroyd, and J. A. Blanco, J. Phys.: Condens. Matter **24**, 213201 (2012).

[75] See Supplemental Material at http://link.aps.org/supplemental/10.1103/PhysRevB.104.134404 for further information on the phonon–band contribution, which includes Ref. [84].

[76] See Supplemental Material at http://link.aps.org/supplemental/10.1103/PhysRevB.104.134404 for various $s_{\text{surface}}(q, \omega)$ contributions.

[77] P. Talagala, P. S. Fodor, D. Haddad, R. Naik, L. E. Wenger, P. P. Vaishnava, and V. Naik, Determination of magnetic exchange stiffness and surface anisotropy constants in epitaxial $Ni_{1-x}Co_x(001)$ films, Phys. Rev. B **66**, 144426 (2002).

[78] D. Rojas, L. F. Barquín, J. S. Marcos, C. Echevarria-Bonet, J. Espeso, J. R. Fernández, L. R. Fernández, and M. Mathon, Magnetic disorder in $TbAl_2$ nanoparticles, Mater. Res. Express **2**, 075001 (2015).

[79] J. Rodriguez-Carvajal, Recent advances in magnetic structure determination by neutron powder diffraction, Phys. B: Condens. Matter **192**, 55 (1993).

[80] A. Tomou, D. Gournis, I. Panagiotopoulos, Y. Huang, G. Hadjipanayis, and B. Kooi, Weak ferromagnetism and exchange biasing in cobalt oxide nanoparticle systems, J. Appl. Phys. **99**, 123915 (2006).

[81] A. H. Morrish, *The Physical Principles of Magnetism* (Wiley Online Library, 2001).

[82] M. Borombaev, R. Levitin, A. Markosyan, V. Rejmer, E. Sinitsyn, and Z. Smetana, Magnetic properties of the $GdCu_2$ single crystal, Zh. Eksp. Teor. Fiz. **93**, 1517 (1987).

[83] M. Bauer, M. S. S.Brooks, and E. Dormann, Orbital polarization of the conduction electrons in ferromagnetically ordered $GdAl_2$, Phys. Rev. B **48**, 1014 (1993).

[84] A. Furrer and H.-G. Purwins, Crystalline electric field in the light (rare-earth)-Pd_3 compounds determined by inelastic neutron scattering, J. Phys. C: Solid State Phys. **9**, 1491 (1976).